The Egyptian Journal of Remote Sensing and Space Sciences 27 (2024) 1–9

Contents lists available at ScienceDirect

The Egyptian Journal of Remote Sensing and Space Sciences

journal homepage: https://www.sciencedirect.com

Research Paper

A machine learning-based method for multi-satellite SAR data integration

Doha Amr [a,*], Xiao-li Ding [a,*], Reda Fekry [b]

[a] Department of land surveying and geo-informatics, The Hong Kong Polytechnic university, Hung Hom, Kowloon, Hong Kong
[b] Department of Geomatics engineering, Faculty of engineering at Shoubra, Benha University, Cairo, Egypt

ARTICLE INFO

Keywords:
Deformation
Multi-band SAR integration
Machine learning
Support vector machine

ABSTRACT

Large- and small-scale subsidence coexist in the world's coastal cities due to extensive land reclamation and fast urbanization. Synthetic aperture radar (SAR) images are typically limited by either low resolution or small coverage, making them ineffective for fully monitoring displacement in coastal areas. In this research, a machine learning-based method is developed to investigate the reclaimed land subsidence based on multi-satellite SAR data integration. The proposed method requires at least a pair of SAR images from complementary tracks. First, the line-of-sight (LOS) displacements are recovered in connection to a series of extremely coherent points based on the differential interferometry synthetic aperture radar (DInSAR). These LOS displacements are then converted into their vertical component, geocoded to a common grid, and simultaneously integrated (i.e., pixel-by-pixel) based on Support Vector Regression (SVR). The proposed methodology does not necessitate the simultaneous processing of huge DInSAR interferogram sequences. The experiments include high-resolution COSMO-SkyMed (CSK) and TerraSAR-X (TSX) images, as well as a small monitoring cycle Sentinel-1 (S1) images of reclaimed territories near Hong Kong Kowloon City. The overall average annual displacement (AAD) ranges from -12.86 to 11.63 mm/year derived from 2008 to 2019. The evaluation metrics including RMSE, MAE, correlation coefficient, and R-squared are used to investigate the impact of SVR in the integration of SAR datasets. Based on these evaluation metrics, SVR is superior in terms of integration performance, accuracy, and generalization ability. Thus, the proposed method has potentially performed multi-satellite SAR data integration.

1. Introduction

In the world's fast-growing mega-cities, ground deformation has increasingly become one of the most common risks to life and property. Artificial activities such as land reclamation, groundwater exploitation, and underground construction are associated with rapid city development, all of which are potential causes of ground deformation (Wu et al., 2021). Initially, traditional field procedures (e.g., leveling and GNSS) have been utilized for deformation monitoring. Notwithstanding, the high reliability of these methods, their main drawbacks are represented by low spatial resolution in large-scale projects, relatively high cost, and lack of manpower. On the contrary, advanced remote sensing techniques particularly differential synthetic aperture radar interferometry (DInSAR) monitor deformation at large-spatial coverage at high levels of accuracy (Gabriel et al., 1989).

Nowadays, there are different bands of available SAR data such as C-band (SIR-C, ERS, ENVISAT, RADARSAT-1/2, and Sentinel-1), X-band (TerraSAR-X and COSMO-SkyMed), L-band (JERS, ALOS-1/2, TerraSAR-L, and DESDynl), and P-band (BIOMASS), have been launched (Brcic et al., 2010). Because the multi-band SAR datasets differ in maximum detection gradient, degree of decorrelation, noise rejection capability, etc., they enable depth interpretation of the surface deformation (Baran et al., 2005). Accordingly, the integration of multiple operational bands, polarimetric channels, and orbit orientations will enrich the gained information (Euillades et al., 2021). For instance, (Pepe et al., 2016) has utilized a time-dependent geotechnical model of the observed deformation to solve a non-linear optimization problem based on the Levenberg-Marquardt method. On the one hand, several approaches have proposed to retrieve the three-dimensional (3D) components of the deformation velocity based on multi-sensor DInSAR (Gray, 2011; Gudmundsson et al., 2002; Hu et al., 2012, 2013; Wright et al., 2004). Lately, a few studies have proposed multi-satellite/multi-angle SAR data combination for long-lasting 3D time-series of ground deformation (i.e., vertical, east-west, and north-south components) (Chang et al., 2018; Hu et al., 2013; Pepe et al., 2016; Samsonov and d'Oreye, 2012b). For example, (Pepe et al., 2015) combined radar LOS-

* Corresponding authors.
E-mail addresses: doha.abdewltawab@feng.bu.edu.eg, dohaa.hassan@connect.polyu.hk (D. Amr), xl.ding@polyu.edu.hk (X.-l. Ding), reda.abdelkawy@feng.bu.edu.eg, fekry.khaliel@connect.polyu.hk (R. Fekry).

https://doi.org/10.1016/j.ejrs.2023.12.001
Received 21 September 2023; Accepted 4 December 2023
Available online 14 December 2023
1110-9823/© 2023 National Authority of Remote Sensing & Space Science. Published by Elsevier B.V. This is an open access article under the CC BY-NC-ND license (http://creativecommons.org/licenses/by-nc-nd/4.0/).

projected time-series of deformation collected by several SAR platforms based on the minimal acceleration (MinA) technique. (Zhao et al., 2019) linked time-overlapped multi-satellite DInSAR deformation time-series over the area of the Eastern coast of Shanghai to produce a long-term displacement time series. (Derauw et al., 2020) proposed an automatic and unsupervised multidimensional time series (MasTer) toolbox based on the multidimensional small baseline subset (MSBAS) method (Samsonov and d'Oreye, 2012a; Samsonov et al., 2017; Samsonov, 2019; Samsonov et al., 2020). Nowadays, a growing interest has been shown in the development of ML to gain useful insights from InSAR data. Their potential performance has been reported in various tasks including object detection, classification of surface displacement, and despeckling (Chang et al., 2018). Therefore, ML algorithms are anticipated to be exploited to integrate SAR data acquired by the next generation of sensors. These sensors hopefully have daily revisiting times (such as those theoretically provided by geosynchronous SAR systems) and could allow InSAR to be used in both the prevention and post-emergency phases of a disaster.

Accordingly, this paper introduces a novel framework for multi-sensor SAR data integration. The proposed method exploits the ML algorithm namely multi-variable SVR. The main advantages of the proposed framework include (1) mitigation of the issues related to processing massive amounts of data in a timely manner, (2) reduction of processing hundreds of differential SAR interferograms simultaneously because it is a post-processing technique and (3) integration of multi-satellite SAR data without extensive adjustment of hyper-parameters. The research contributions are summarized in:

- development a new DInSAR ML-based combination technique using SVR.
- comprehensive statistical analysis of the combined DInSAR products.
- providing a unique solution and it is anticipated to be more robust with less time-overlapping between multiple SAR datasets.

This paper is structured as follows: Section 2 presents the study site and dataset included in this study. Section 3 provides an overview of the research methodology. Next, the experiments and research findings with deep interpretation are presented in Section 4 and Section 5. Finally, the research conclusions are summarized in Section 6.

2. Materials

2.1. Study area

Kowloon peninsula is the study area of this research. It is the most populous district of Hong Kong, China (Qin and Perissin, 2015). Because the land in Hong Kong is scarce and valuable, the government has been reclaiming land from the sea to construct skyscrapers, ports, airports, etc., Monitoring the subsidence of reclaimed lands for a long time and with precision can help to avoid geological hazards and financial loss. Fig. 1 shows the location of the Kowloon district on the Hong Kong map.

Several stages of land reclamation from the sea have resulted in a significant expansion of the peninsula, as shown in Fig. 2. Most of the south and west reclamation was completed before 1904. By 1982, numerous other tiny portions along the main Tsim Sha Tsui shoreline had been reclaimed. Parts of Hung Hom Bay have been reclaimed since 1994, and it was fully depleted by 2019. The Airport Core Programme created the West Kowloon Reclamation, which was substantially completed by 1995. Long periods of subsidence are common on reclaimed land, which can compromise building structures and subterranean infrastructures like water and sewage systems. In Hong Kong, ground deformation has long been an issue, particularly on the reclaimed territory from the sea (Chen et al., 2010).

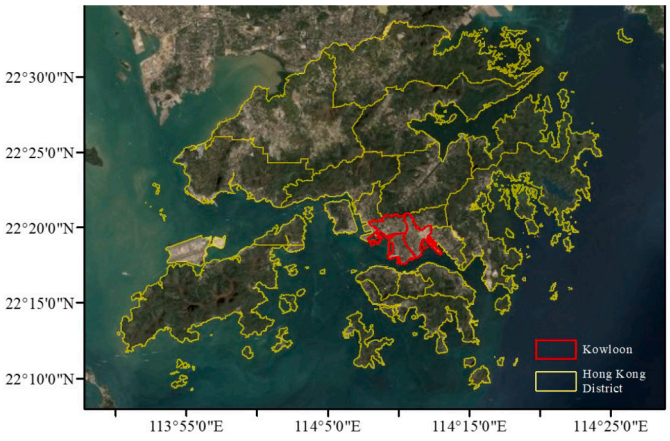

Fig. 1. Location of Kowloon area framed by the red color.

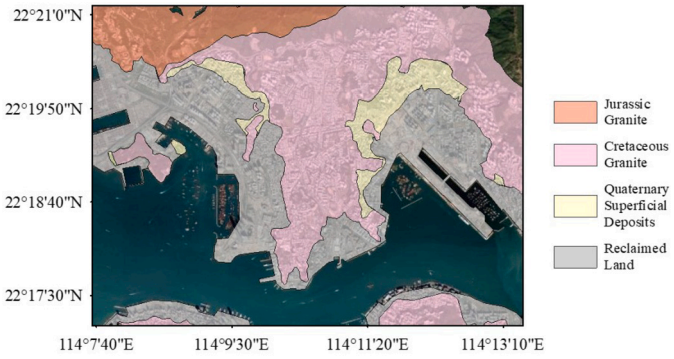

Fig. 2. Geological map and reclamation land within the study area.

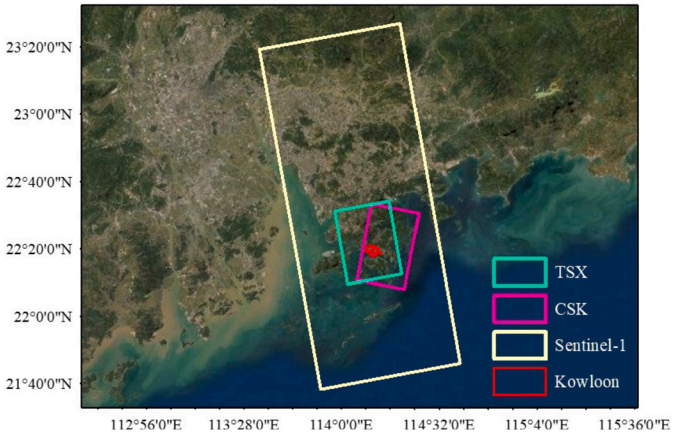

Fig. 3. SAR data coverage for the study area.

2.2. Dataset

Multi-satellite SAR datasets over the Kowloon area were collected, as described in Table 1. To carry out an extensive examination of the mechanisms of deformation over the Kowloon Peninsula, three separate sets of SAR data, each with a distinct band of frequency, were chosen. Fig. 3 illustrates the coverage of the SAR datasets. It is worth noting that the three sets of SAR data are clearly time-overlapping.

3. Methodology

The proposed methodology combines several multi-sensor DInSAR data to generate long-term ground deformation maps using SVR. Vertical displacements are computed individually for all datasets based on

Table 1
Characteristics of the selected SAR data.

Satellite	TerraSAR-X (TSX)	COSMO-SkyMed (CSK)	Sentinel-1 (Path_11)		
			Frame_67	Frame_68	Frame_69
Orbital	Ascending	Descending	Ascending	Ascending	Ascending
Period	20081025–20170125	20160829–20190204	20151212–20160504	20160516–20170228	20150709–20151013
No. of image	130	16	8	18	9
Polarization	VV	HH	VV	VV	VV
Incidence angle	37°	38°	37.5°	37.5°	37.5°
Band	X	X	C	C	C
Wavelength (cm)	3.1	3.6	5.6	5.6	5.6

the DInSAR technique. After that, these displacements are integrated based on the SVR algorithm The following subsections explain the detailed steps of the proposed methodology.

3.1. DInSAR processing

A set of m multiple-master small baseline interferograms was formed based on the three SAR datasets. A threshold of perpendicular and temporal baselines was implied to reduce the occurrence of temporal and spatial phase decorrelation components in the generated interferograms and improve the coherence of the processed pixels' phase quality. Data pre-processing for each SAR dataset is performed with GAMMA software (Werner et al., 2000), which comprises SAR image extraction, co-registration, interferogram generation, and flat-earth phase and topographical phase removal. Multi-looking in the range and azimuth directions, and phase filtering were carried out to suppress speckle noise and improve the signal-to-noise ratio. For phase unwrapping, the minimal cost flow network and Delaunay 3D are used, with a coherence threshold of 0.30. A linear empirical function is used to estimate the phase ramps induced by orbital errors and atmospheric delays. Until then, the residual topography is removed as well. After that, the atmospheric phase was filtered. Next, geocoding in the LOS direction with a 10-meter resolution is used. Finally, the displacement rate is calculated and mapped across the research area. All available displacement values must initially be converted to vertical (subsidence or uplift) values before the proposed multi-band combination approaches can be implemented. For each well-processed point, LOS-projected ground displacement d_{LOS} generated via the DInSAR process is easily converted to vertical movements d_u using the incidence angle θ such that:

$$d_u = \frac{d_{LOS}}{\cos\theta} \tag{1}$$

3.2. Multi-satellite SAR-ML based merging algorithm

SVR performed effectively in estimating real functions with great generalization and high predictive accuracy (Gupta et al., 2015). Consequently, SVR has been adapted for multi-band vertical displacement integration.

3.2.1. Support vector regression

SVR is a statistical theory-based data mining method that is an extension of SVM for regression analysis. When given an input value, SVR searches for a function that can predict the continuous output value most accurately. SVR architecture is similar to artificial neural networks as shown in Fig. 4. Input and output layers are connected by a hidden layer that is self-computed using the input data. SVR maps the feature vectors of sample data into high dimensional space and the regression is employed based on the kernel function as depicted in Fig. 5.

Let $f(x) = \omega \times x + b$ be an SVR function that is defined by a coefficient ω, the input feature vector x; and the bias constant b therefore, the most valuable regression function is obtained by creating a minimization function as follows:

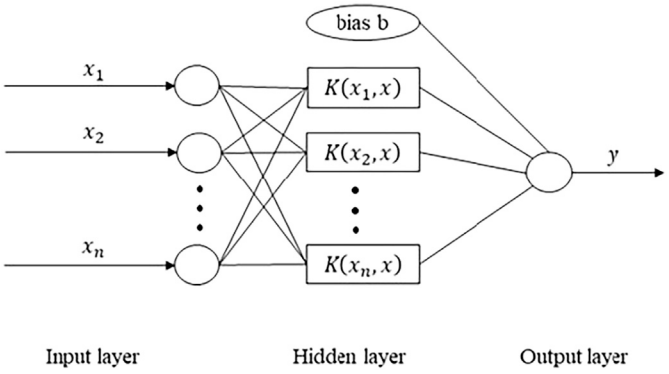

Fig. 4. SVR structure.

$$min\frac{1}{2}\omega^T\omega + c\frac{1}{N}\sum_{i=1}^{N} L(f(x_i), y_i) \tag{2}$$

$$L(y) = \begin{cases} 0, & \text{if } |f(x_i) - y_i| < \epsilon \\ |f(x_i) - y_i| - \epsilon, & \text{if } |f(x_i) - y_i| > \epsilon, \end{cases} \tag{3}$$

where c is the penalty factor, N is the sample's number, $f(x_i)$ is the predicted value of the i^{th} feature vector, y_i is the true value of i^{th} feature vector, L is the linear insensitive loss function, and ϵ is the maximum deviation. The Lagrange equation and the Karush-Kuhu-Tucker condition are employed to derive the dual mode of the SVR model and calculate the partial derivatives of the parameters (Duan et al., 2018). The final decision function is:

$$f(x) = \sum_{i=1}^{l}(\alpha_i^* - \alpha_i)K(x_i, x) + b, \tag{4}$$

such that l represents the amount of SVR machines; α_i is the optimum solution; K represents the kernel function in the nonlinear regression, $K(x_i, x) = \Phi(x_i) * \Phi(x_j)$. In order to effectively avoid the issue of dimensional explosion in a high-dimensional space, a better kernel function has been chosen and the output is transferred to a high-dimensional space by computing in a low-dimensional space. Radial basis function (RBF) was utilized because of its potential performance in nonlinear regression of engine response. It has high flexibility based on kernel function coefficient γ:

$$k(x_i, x_j) = exp(-\gamma|x_i - x_j|^2), \gamma > 0 \tag{5}$$

This paper utilized multiple independent variables SVR to integrate three sets of time-overlapped TSX, CSK, and S1 DInSAR vertical displacement over common high-coherent points. The response parameter $y = d_u^1, d_u^2, ..., d_u^m$ is the geocoded vertical ground displacement determined regarding a specific point from high-coherent points. The training set $x = (C^1, T^1), (C^2, T^2), ..., (C^m, T^m)$ is the combined vector of all the two input process parameters (coherence value at each point in each interferogram (C), and time span (T) of each interferogram (in days)). SVR employs m sets of input-output pairings and the training procedure

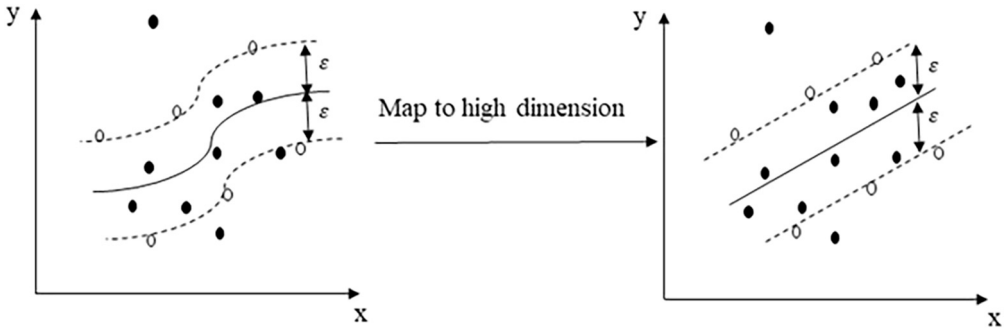

Fig. 5. Schematic diagram of the kernel trick.

Table 2
Perpendicular and temporal baselines threshold of the three SAR datasets.

Satellite	TerraSAR-X (TSX)	COSMO-SkyMed (CSK)	Sentinel-1 (Path_11)		
			Frame_67	Frame_68	Frame_69
Perpendicular baseline	150	1200	95	95	95
Temporal baseline	365	900	150	150	120

was carried out to obtain the ideal parameters. A combined multi-band displacement is then obtained using these parameters.

3.3. Evaluation metrics

Four metrics were utilized to evaluate the SVR model performance in multi-band displacement integration the Root-Mean-Square Error $RMSE = \sqrt{\frac{1}{n}\sum_{i=1}^{n}(y_i^P - y_i^O)^2}$, Mean Absolute Error $MAE = \frac{1}{n}\sum_{i=1}^{n}|y_i^P - y_i^O|^2$, Correlation Coefficient $r = \frac{\sum(y_i^O - \overline{y}^O)-(y_i^P - \overline{y}^P)}{\sqrt{\sum(y_i^O - \overline{y}^O)^2-(y_i^P - \overline{y}^P)^2}}$, R-squared R^2 where n is the total number of observations y^O or predictions y^P in the testing period. Also, $\overline{y}^O$ and $\overline{y}^P$ are the averages of the observed and predicted values, respectively.

4. Results

4.1. Interferogram generation

DInSAR technique was applied to C- and X-band SAR images, particularly, selected image pairs based on the perpendicular and temporal baseline threshold as shown in Table 2. Accordingly, 1180, 98, and 181 interferograms were created from the TSX, CSK, and S1 datasets, respectively. Fig. 6 elucidates the configuration of the baseline of interferometric networks for individual datasets.

Across the entire monitored period, the small baselines describing the accessible scenes exhibited good density and redundancy, and all the scenes were used for DInSAR analysis. The image pairs were co-registered and the phase difference is computed to generate DInSAR. Then, A DEM from SRTM was used for topographic phase removal. A complex multi-look operation was then independently carried out to mitigate the effects of the decorrelation noise (with 5 looks in azimuth and range directions for the TSX, with 5 looks in azimuth, and 4 looks in range direction for the CSX, and with 10 looks in azimuth, and 2 looks in range for the S1). Additionally, noise filtering was employed for single interferograms. Next, phase unwrapping was performed using the extended minimum cost Flow algorithm. It is worth noting that incoherent and sea areas were automatically masked off because only the set of coherent pixels common to all interferograms was used for phase unwrapping. Moreover, the unwrapped phase was calibrated to a unique ground reference point that was considered to be stable. Finally, the unwrapped phase was converted into LOS displacements and a map of the average LOS deformation velocity was generated from each SAR dataset. LOS-projected deformation datasets were transformed to a vertical (up-down) direction before integration using Equation (1).

4.2. Vertical displacement

The vertical displacement velocities were displayed on a grid of highly coherent pixels that were common in the three datasets, described as those with a temporal coherence larger than 0.8, to assure accurate results. The number of selected coherent points was different for all datasets because the highest observing range is directly proportional to the radar wavelength. Accordingly, a larger number of points was identified for Sentinel-1 data. C-band radar wave, (longer wavelength than the X-band) has a superior probability of detecting large-gradient deformation. Fig. 7 demonstrates that from 2008 to 2017, the AAD varies between -12.38 and 11.12 mm/year. Fig. 8 8a, b, and c, respectively, elucidate the AAD in the vertical direction for the X-band TSX, X-band CSK, and C-band Sentinel-1 datasets before integration. The selected high-coherence points gradually turn from blue to red, signaling an increase in subsidence values. The three datasets were resampled to the same resolution in order to make them comparable and consistent for upcoming processing.

According to TSX data from 2008 to 2017, the ground displacement across Kowloon ranges from -9.72 to 6.25 mm/year. Moreover, a maximum subsidence rate of -8.49 mm/year is depicted on the CSK displacement map from 2016 to 2019 as shown in Fig. 8b. The AAD ranges from -9.19 to 9.82 mm/year from 2015 to 2017, as demonstrated by a Sentinel-1 displacement map in Fig. 8c. The ground displacement is primarily located along the top and western borders of the Kowloon in the three displacement maps. Due to the fact that a piece of the Kowloon Peninsula has been reclaimed from the sea, the non-reclamation region is utilized as the reference area (white rectangle in Fig. 8) for all datasets, and the reference point is identified at the highest coherence.

4.3. Fusion results of TSX, CSK, and S1 datasets

The integration results compensate for the shortcomings of individual datasets because the map reflects both the TSX's, CSK's high resolution, and Sentinel-1's enhanced observing capability. Positive values (blue) represent ground uplift, and negative values (red) present ground subsidence. Fig. 9 elucidates the integration results of the TSX, CSK, and Sentinel-1 data. The average annual velocity ranged from -12.86 to 11.63 mm/year. The displacement behavior and magnitudes computed from the three datasets closely match previous research in this area (Wu et al., 2021).

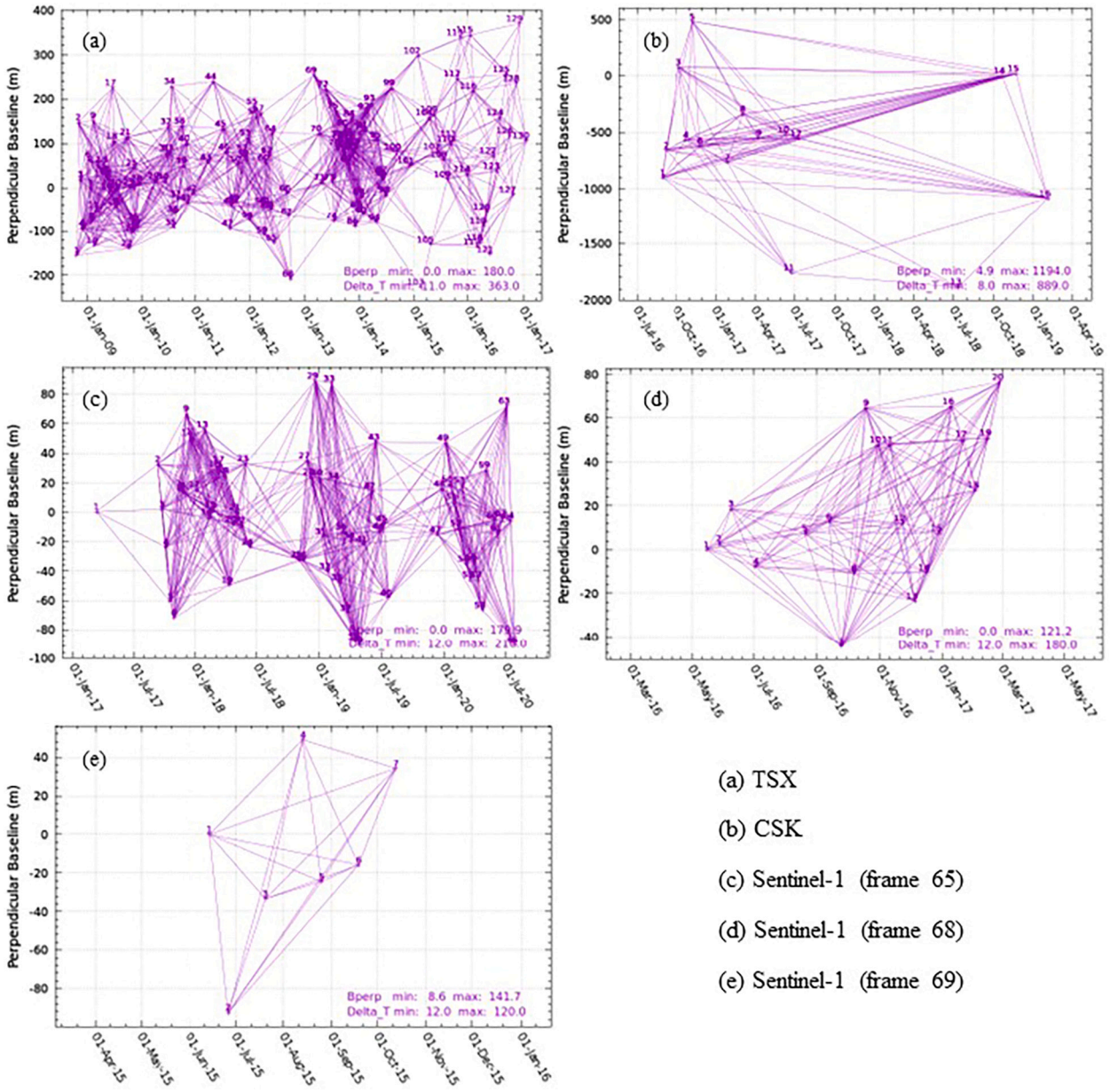

Fig. 6. Baseline configuration of TSX, CSK, and Sentinel-1A datasets.

Table 3
Performance of the SVR-based Integration model.

Evaluation Index (mm/year)	value
$RMSE$	1.12
MAE	0.88
Correlation coefficient (r)	0.97
R-squared	0.95
Standard deviation (STD)	0.69

4.3.1. SVR validation results

SVR integration results were validated according to the scheme described in Section 3.3. $RMSE$, MAE, correlation coefficient, and R-squared are computed as summarized in Table 3. Fig. 10 elucidates the scatter map between AAD from stacking all interferograms of TSX, CSK, and S1 and the SVR-based integration model. It is found that the two datasets have a consistent deformation pattern.

According to the statistical evaluation parameters, the results demonstrated that the SVR soft computing model is superior in terms of integration performance, accuracy, and generalization capability. SVR thus offers potential in multi-satellite SAR data integration and related fields.

4.3.2. Cross validation results

First, TSX and Sentinel-1 SAR datasets were used for cross-validation as (Wu et al., 2021), which were obtained in ascending directions and have the same geometry. The displacement velocity maps of the two data over the Kowloon area from the same period (2015-2017) were extracted, before applying the proposed integration method. To validate the derived displacement, the differences between the two datasets (Δd_{TSX-S1}) were calculated as illustrated in Table 4 where the vertical displacement velocity maps are resampled into a common grid.

The normality of the distribution of the difference between the two dataset's results is examined using a quantile-quantile (q-q) plot and histogram for ADD resulting from both datasets for the period 2015 to 2017, as shown in Fig. 11 a and b, respectively.

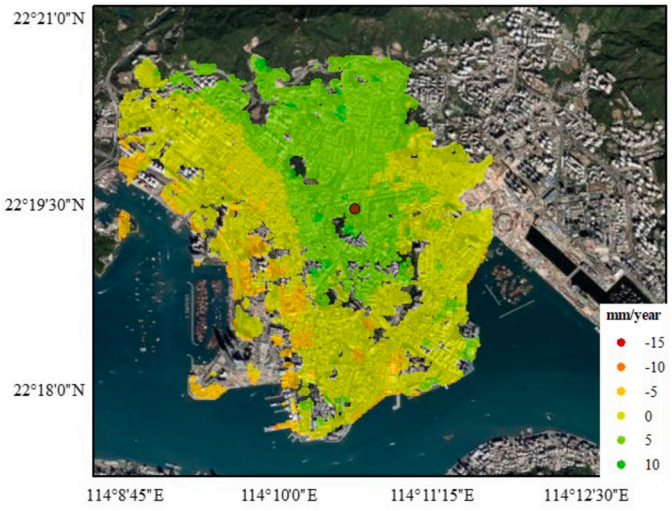

Fig. 7. AAD of Kowloon from 2008 to 2017 by stacking all multi-baseline interferograms of TSX, CSK, and S1 datasets.

Table 4
Difference between AAD obtained from TSX and S1.

Evaluation index (mm/year)	Δd_{tsx-s1}	
	Pre	Post
Mean	7.15	5.44
Median	6.05	4.87
STD	4.99	3.78
$RMSE$	8.72	6.62

Table 5
Cross-validation for each dataset before and after SVM-based integration.

Evaluation index/ Satellites	TSX	CSK	S1
Mean	0.97	1.19	3.61
STD	0.71	1.1	3.28
Median	0.93	0.78	2.31
$RMSE$	1.53	1.42	4.28

In the right side and center of Fig. 11 a, there is an almost-perfect normal distribution. The tails, particularly those on the left, show large departures from the normal distribution; the histogram, Fig. 11 b, shows that the distribution on the left is right-skewed. These departures could be related to the uncertainty in the SAR dataset, as well as atmospheric delay and acquisition time. The (Δd_{TSX-S1}) before and after integration were compared and described by box plots as shown in Fig. 12. Fig. 12 demonstrates that the distribution is biased toward lower values and the mean is more positive than the median, as shown by the boxplot graph, which will automatically identify the min/max range, 75 percent quantile range, mean value, and outliers. The $RMSE$ values are 8.72 and 6.62, and the standard deviations are 4.99 and 3.78 mm/year before and after integration, respectively. After using the ML-based integration method, the results have shown a greater improvement.

Second, a quantitative study of the differences between the displacement velocities obtained before and after SVM-based integration, as shown in Table 5, was applied to validate integration-derived displacement for each dataset (TSX, CSK, S1) separately. Fig. 13 represents a comparison of the differences in measured displacement velocities of the three datasets' boxplots.

Mean, median, $RMSE$, and standard deviation of the displacement velocity differences were listed in Table 5. TSX provides a lower mean difference than the S1 and CSK, with values of 0.97, 1.19, and 3.61 mm/year, respectively. In addition, when compared to CSK and S1, TSX has the best standard deviation and $RMSE$ values. These $RMSE$ values elucidate that the TSX results were better than the CSK and S1 results. This could be attributed to the larger number of TSX interferograms involved in the integration process than the number of interferograms involved with CSK and S1.

Table 6
Standard deviations and $RMSE$ of the differences between the three frame datasets before and after integration.

Evaluation index/ Frames	67-68		68-69		69-70	
	Pre	Post	Pre	Post	Pre	Post
Mean	4.52	1.21	6.80	1.70	7.99	1.29
Median	3.98	1.14	5.12	1.44	6.60	0.76
STD	3.30	0.75	5.91	1.54	6.58	1.60
$RMSE$	5.60	1.43	9.02	2.29	10.35	2.05

Third, the results from different S1 datasets generated from different frames were cross-validated as (Ng et al., 2012; Jiang and Lin, 2010) to study the effect of the SVM-based integration on the relation between different frames of S1 datasets as in Table 6. The standard deviations and $RMSE$ of the differences between the three frame datasets before and after integration are determined.

The $RMSE$ values are 5.60, 9.02, 10.35, and 1.43, 2.29, 2.05, and the standard deviations are 3.30, 5.91, 6.58, and 0.75, 1.54, 1.60 mm/year before and after integration, respectively, demonstrating excellent improvements among the results after applying the ML-based integration method.

5. Discussion

5.1. SVM for multi-sensor SAR data integration

The proposed framework depends mainly on SVR to integrate multi-satellite SAR data. SVR is based on statistical learning theory and has the following characteristics: (1) a learning method derived from the structural risk reduction principle governs the trade-off between regression accuracy and regression hyperplane complexity; (2) it converts actual problems into a high-dimensional feature space, allowing nonlinear aspects to be represented using linear operators; (3) model can be solved using convex quadratic programming, with the global optimal solution theoretically preserved; (4) and the formulation of the load regression function is defined by only a few support vectors rather than the full sample set overcoming the dimensionality curse (Liu et al., 2021). Our proposed method is post-processing, therefore it does not necessitate handling hundreds of differential SAR interferograms simultaneously and it exploits the technological advancements made in the creation of LOS in recent years. Integration of multi-satellite deformation components is mainly affected by information on the quality of LOS displacement and the determination of very coherent targets common to all datasets. Any disturbance in the LOS displacement can be estimated and filtered before integration preventing error propagation during integration. Our experimental results showed that ML has potentially performed while the integrated displacements are determined to sub-millimeter-level precision which is comparable to those from LOS displacements. Accordingly, the proposed method is expected to perform well in investigating geological and geophysical processes where deformation discrimination is a major concern.

5.2. Land subsidence based on multi-sensor SAR data

Currently, there is an increasing number of satellite data vendors. This includes the latest C, X, and L-band SAR imagery from SAR sensors (such as RADARSAT-2, Sentinel-1A, ALOS-2, TerraSAR-X, Tandem-X, and the COSMO-SkyMed constellation) as well as SAR sensors (such as ENVISAT and ERS). Therefore, it becomes possible to track the ongoing surface displacements from a regional level to small structures. In this

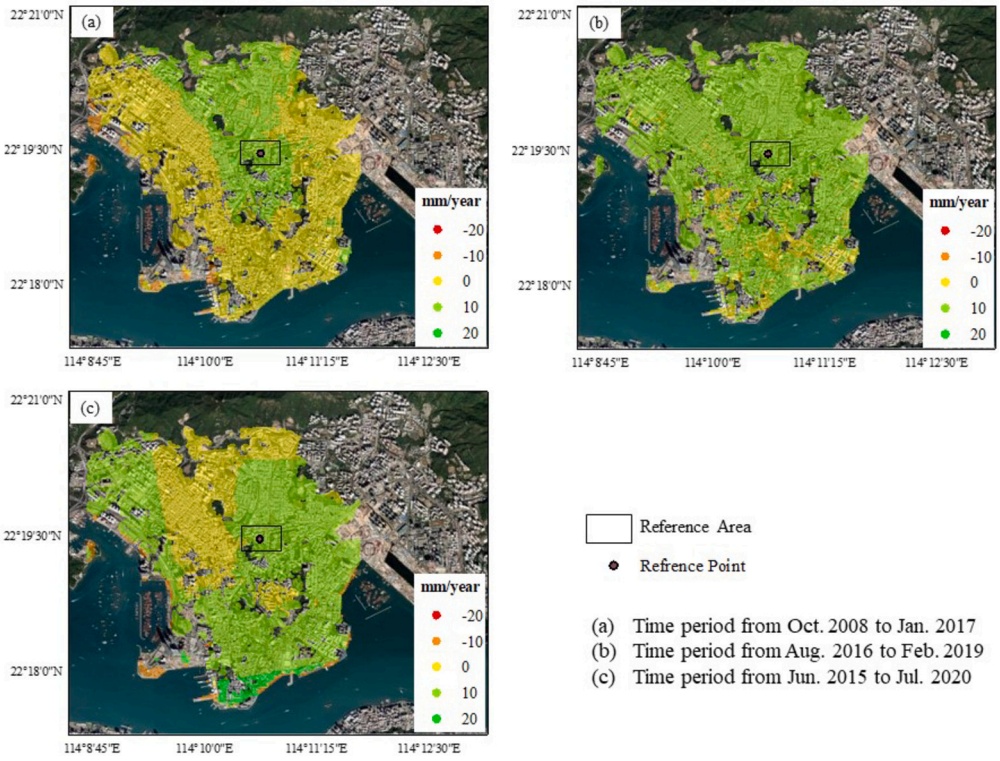

Fig. 8. AAD maps of Kowloon. (a) TSX. (b) CSK. (c) Sentinel-1A.

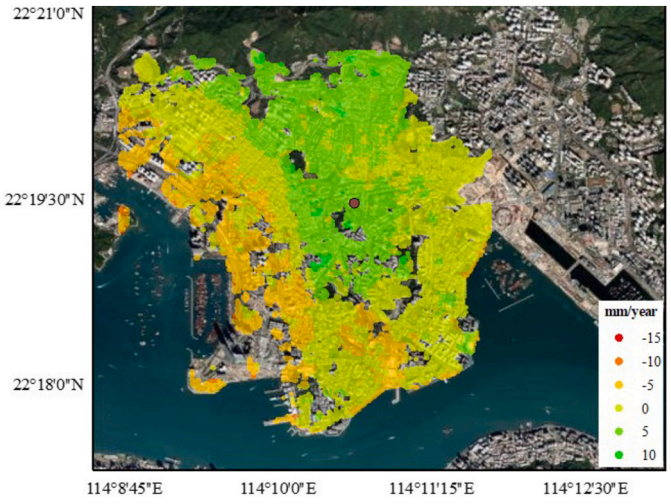

Fig. 9. Combined AAD map resulted from SVM-based integration of TSX, CSK, and S1 datasets.

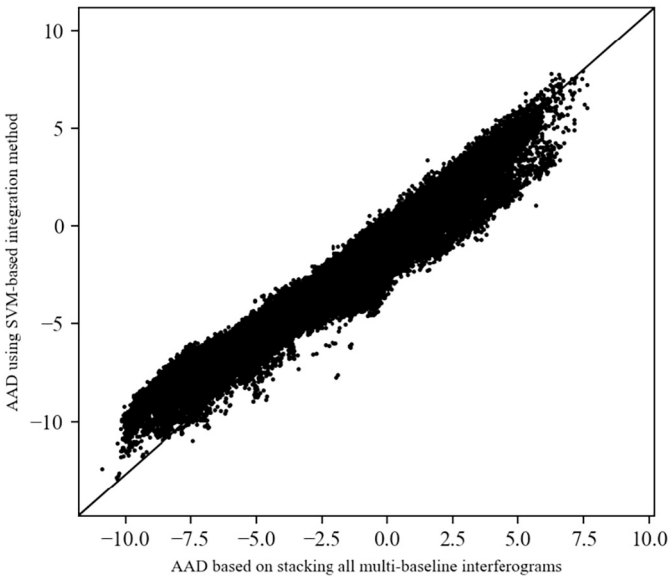

Fig. 10. Scatter map of AAD pre and post SVM-based integration.

paper, three separate SAR datasets, the TSX, CSK, and S1, were utilized to study long-term ground subsidence. From the band point of view, C-band has a superior ability to monitor displacement whereas shorter wavelength and lower frequency bands (e.g., x-band) allow for more comprehensive coverage of natural regions and less temporal decorrelation. These satellites capture data over a lengthy period of time, allowing us to track long-term deformation. The utilization of an uneven number of images and varying imaging properties make assessing their performance challenging. Even though, the short revisit period of TSX and S1 enabled the observation of short-term land deformations due to human activities. Moreover, the overlap between the three datasets encouraged the integration of multi-sensor InSAR results. Further, the cross-heading tracks of the TSX and CSK images identified deformation on both sides, implying that the cross-heading tracks facilitated thorough displacement determination in the research area. In conclusion, the combined multi-sensor SAR data illustrates the feasibility of continuous deformation surveillance.

5.3. Local reclamation settlement, possible causes, and implications

The three mechanisms that cause natural consolidation of reclamation fills are (a) primary consolidation (3 years after reclamation); (b) long-term second compression of the alluvial clay deposits beneath the reclamation; (c) creep within the reclamation fill (over 40 years after reclamation). As per Ma et al. (2019), fill variability impacts consolidation variability and creates unequal settlement. Ground deformation is

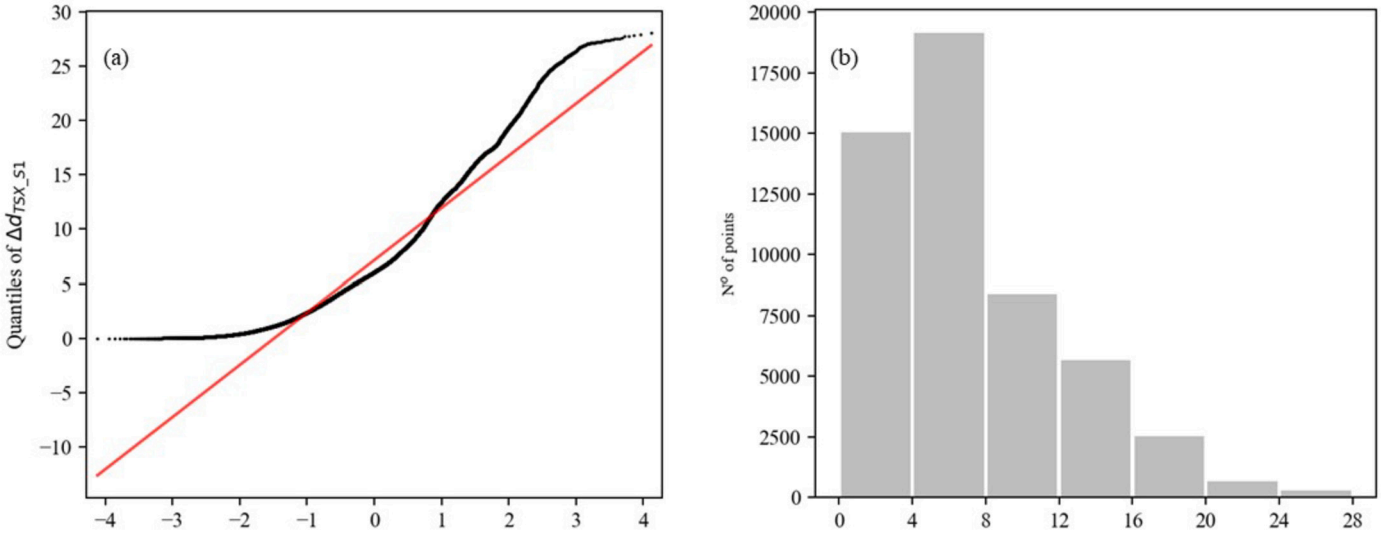

Fig. 11. Quantile-quantile (q-q) plot and histogram of Δd_{TSX-S1} from 2015 to 2017.

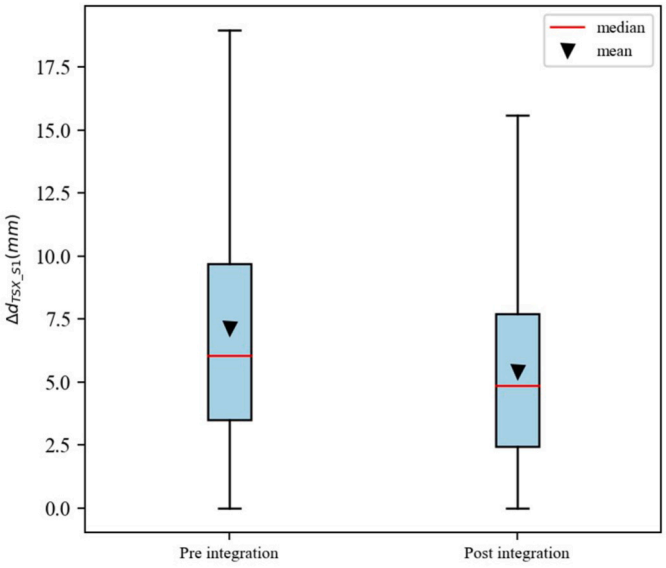

Fig. 12. Box-plots of (Δd_{TSX-S1}) before and after applying the SVM-based integration method.

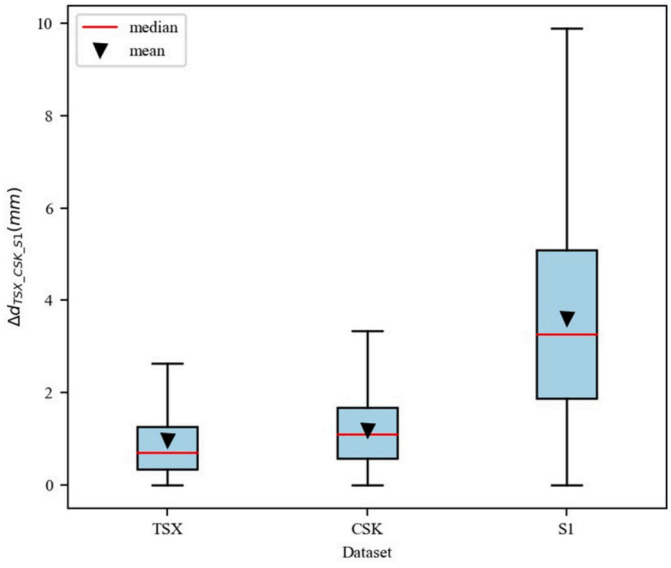

Fig. 13. Box plots of the difference between AAD from TSX, CSK, and S1 before and after the SVM-based integration.

discovered by examining geological formations (see Fig. 2) and human activities that always reinforce each other. The study area is formed of granites, alluvium/colluvium, and reclamation land. Granite is a type of intrusive igneous rock that is known for being a relatively stable stratum whereas surrounding reclaimed land is less stable. Preceding research has revealed ground displacement on reclaimed land in various locations of Hong Kong (Ding et al., 2004). For instance, human activities, (e.g., the vast underground train system in the west corridor) represent a reason for ground displacement. Also, sinking and building cracks have been reported by Qin and Perissin (2015). Therefore, the interaction between the geological structure and subterranean projects is most likely to blame for the concentrated ground displacement in this location. Long-term large-scale subsidence increases the risk of flooding and saltwater intrusion as sea levels rise (Dang et al., 2018). Buildings and infrastructures are being threatened by small-scale subsidence which poses a greater hazard to humans than regional sediment subsidence. The reason is it occurs frequently in densely populated places and its vast dispersion, invisibility, rapid occurrence, and complex creation (Ma et al., 2019). Local governments are becoming increasingly concerned about the considerable impact of small-scale subsidence.

On the other hand, validation showed that the developed approach recorded sub-millimeter-level accuracy in integrating multi-satellite SAR datasets. It enables the one-by-one integration of interferograms (from different sensors and viewing orientations as they become available) resulting in 1-D displacements at each SAR interferogram time. An essential advantage of the developed approach is achieving significantly higher observation resolution by combining measurements from various radar sensors. Therefore, the multi-satellite SAR-ML-based integration method is expected to be effective in analyzing geological and geophysical processes however, in-depth evaluations are required to clarify and evaluate the proposed method's potential. This necessitates the utilization of a similar number of images from each SAR satellite data testing the developed approach in various situations. Moreover, utilizing multi-platform SAR data to retrieve a multi-dimensional deformation map to monitor deformation anomalies. Further, the developed methodology preserves TerraSAR-X's and COSMO-SkyMed's high resolution and Sentinel-1's better monitoring ability while also decreasing the monitoring cycle. Furthermore, Hong Kong's Kowloon district is one of the city's most populous. Consequently, the achieved results produced are

a valuable resource for disaster prevention, and widespread planning, urbanization, and land reclamation in this region.

6. Conclusions

This research proposed a novel framework to integrate multi-sensor, multi-track DInSAR measurements using an ML strategy. The experimental results showed that the deformation rates of the Kowloon district range from - 12.86 to 11.63 mm/year. Moreover, the trends of displacement in the west corridor were more than 5 mm/year due to the reclamation of land and the ongoing underground/ground construction projects. Owing to RMSE the SVR-based integration reported a sub-millimeter level of accuracy where the RMSE was 1.12 mm/year. Therefore, the proposed framework has potentially performed on multi-satellite SAR data integration due to one-by-one interferogram integration however, in-depth evaluations are required to clarify and evaluate the proposed method's potential. Moreover, an additional sort of measurement (GPS, leveling) should be used to assess, calibrate, and evaluate the proposed developed framework.

Declaration of competing interest

The authors certify that they have no known competing financial interests or personal relationships that could have appeared to influence the work reported in this paper.

References

Baran, I., Stewart, M., Claessens, S., 2005. A new functional model for determining minimum and maximum detectable deformation gradient resolved by satellite radar interferometry. IEEE Trans. Geosci. Remote Sens. 43, 675–682. https://doi.org/10.1109/TGRS.2004.843187.

Brcic, R., Parizzi, A., Eineder, M., Bamler, R., Meyer, F.J., 2010. Estimation and compensation of ionospheric delay for sar interferometry. In: 2010 IEEE International Geoscience and Remote Sensing Symposium, pp. 2908–2911.

Chang, L., Dollevoet, R., Hanssen, R., 2018. Monitoring line-infrastructure with multisensor sar interferometry: products and performance assessment metrics. IEEE J. Sel. Top. Appl. Earth Obs. Remote Sens. 11, 1593–1605. https://doi.org/10.1109/JSTARS.2018.2803074.

Chen, Q., Liu, G., Ding, X., Hu, J., Yuan, L., Zhong, P., Omura, M., 2010. Tight integration of gps observations and persistent scatterer insar for detecting vertical ground motion in Hong Kong. Int. J. Appl. Earth Obs. Geoinf. 12, 477–486. https://doi.org/10.1016/j.jag.2010.05.002.

Dang, T.D., Cochrane, T.A., Arias, M.E., Tri, V.P.D., 2018. Future hydrological alterations in the Mekong Delta under the impact of water resources development, land subsidence and sea level rise. J. Hydrol. Reg. Stud. 15, 119–133. https://doi.org/10.1016/j.ejrh.2017.12.002.

Derauw, D., d'Oreye Nicolas Jaspard, M., Caselli, A., Samsonov, S., 2020. Ongoing automated ground deformation monitoring of domuyo - laguna del maule area (Argentina) using sentinel-1 msbas time series: methodology description and first observations for the period 2015–2020. J. South Am. Earth Sci. 104, 102850. https://doi.org/10.1016/j.jsames.2020.102850.

Ding, X., Liu, G., Li, Z., Li, Z., Chen, Y., 2004. Ground subsidence monitoring in Hong Kong with satellite sar interferometry. Photogramm. Eng. 70, 1151–1156. https://doi.org/10.14358/PERS.70.10.1151.

Duan, H., Huang, Y., Mehra, R.K., Song, P., Ma, F., 2018. Study on influencing factors of prediction accuracy of support vector machine (svm) model for nox emission of a hydrogen enriched compressed natural gas engine. Fuel 234, 954–964. https://doi.org/10.1016/j.fuel.2018.07.009.

Euillades, P., Euillades, L., Pepe, A., Mastro, P., Falabella, F., Imperatore, P., Tang, Y., Rosell, P., 2021. Recent advancements in multi-temporal methods applied to new generation sar systems and applications in South America. J. South Am. Earth Sci. 111, 103410. https://doi.org/10.1016/j.jsames.2021.103410.

Gabriel, A.K., Goldstein, R.M., Zebker, H.A., 1989. Mapping small elevation changes over large areas: differential radar interferometry. J. Geophys. Res. 94, 9183–9191.

Gray, L., 2011. Using multiple radarsat insar pairs to estimate a full three-dimensional solution for glacial ice movement. Geophys. Res. Lett. 38. https://doi.org/10.1029/2010GL046484.

Gudmundsson, S., Sigmundsson, F., Carstensen, J.M., 2002. Three-dimensional surface motion maps estimated from combined interferometric synthetic aperture radar and gps data. J. Geophys. Res., Solid Earth 107. https://doi.org/10.1029/2001JB000283. ETG 13–1–ETG 13–14.

Gupta, Amit Kumar, Chandra, G.S., Desu, R.K., Balu, A., 2015. Optimisation of turning parameters by integrating genetic algorithm with support vector regression and artificial neural networks. Int. J. Adv. Manuf. Technol. 77, 331–339. https://doi.org/10.1007/s00170-014-6282-9.

Hu, J., Ding, X.L., Li, Z.W., Zhu, J.J., Sun, Q., Zhang, L., 2013. Kalman-filter-based approach for multisensor, multitrack, and multitemporal insar. IEEE Trans. Geosci. Remote Sens. 51, 4226–4239. https://doi.org/10.1109/TGRS.2012.2227759.

Hu, J., Ding, X.L., Li, Z.W., Zhu, J.J., Sun, Q., Zhang, L., Omura, M., 2012. A Kalaman filter based MTInSAR methodology for deriving 3D surface displacement evolutions. In: Ouwehand, L. (Ed.), Fringe 2011, p. 79.

Jiang, L., Lin, H., 2010. Integrated analysis of sar interferometric and geological data for investigating long-term reclamation settlement of chek lap kok airport, Hong Kong. Eng. Geol. 110, 77–92. https://doi.org/10.1016/j.enggeo.2009.11.005.

Liu, Y., Wang, L., Gu, K., 2021. A support vector regression (svr)-based method for dynamic load identification using heterogeneous responses under interval uncertainties. Appl. Soft Comput. 110, 107599. https://doi.org/10.1016/j.asoc.2021.107599.

Ma, P., Wang, W., Zhang, B., Wang, J., Shi, G., Huang, G., Chen, F., Jiang, L., Lin, H., 2019. Remotely sensing large- and small-scale ground subsidence: a case study of the Guangdong–Hong Kong–macao greater bay area of China. Remote Sens. Environ. 232, 111282. https://doi.org/10.1016/j.rse.2019.111282.

Ng, A.H.M., Ge, L., Li, X., Zhang, K., 2012. Monitoring ground deformation in Beijing, China with persistent scatterer sar interferometry. J. Geod. 86, 375–392.

Pepe, A., Bonano, M., Zhao, Q., Yang, T., Wang, H., 2016. The use of c-/x-band time-gapped sar data and geotechnical models for the study of Shanghai's ocean-reclaimed lands through the sbas-dinsar technique. Remote Sens. 8. https://doi.org/10.3390/rs8110911.

Pepe, A., Solaro, G., Dema, C., 2015. A minimum curvature combination method for the generation of multi-platform DInSAR deformation time-series. In: Ouwehand, L. (Ed.), FRINGE 2015, p. 9.

Qin, Y., Perissin, D., 2015. Monitoring ground subsidence in Hong Kong via spaceborne radar: experiments and validation. Remote Sens. 7, 10715–10736. https://doi.org/10.3390/rs70810715.

Samsonov, S., 2019. Three-dimensional deformation time series of glacier motion from multiple-aperture dinsar observation. J. Geod. 93, 2651–2660. https://doi.org/10.1007/s00190-019-01325-y.

Samsonov, S., Dille, A., Dewitte, O., Kervyn, F., d'Oreye, N., 2020. Satellite interferometry for mapping surface deformation time series in one, two and three dimensions: a new method illustrated on a slow-moving landslide. Eng. Geol. 266, 105471. https://doi.org/10.1016/j.enggeo.2019.105471.

Samsonov, S., d'Oreye, N., 2012a. Multidimensional time-series analysis of ground deformation from multiple InSAR data sets applied to Virunga Volcanic Province. Geophys. J. Int. 191, 1095–1108. https://doi.org/10.1111/j.1365-246X.2012.05669.x.

Samsonov, S., d'Oreye, N., 2012b. Multidimensional time-series analysis of ground deformation from multiple insar data sets applied to Virunga volcanic province. Geophys. J. Int. 191, 1095–1108. https://doi.org/10.1111/j.1365-246X.2012.05669.x.

Samsonov, S., Feng, W., Peltier, A., Geirsson, H., d'Oreye, N., Tiampo, K., 2017. Multidimensional small baseline subset (msbas) for volcano monitoring in two dimensions: opportunities and challenges. Case study piton de la fournaise volcano. J. Volcanol. Geotherm. Res. 344, 121–138. https://doi.org/10.1016/j.jvolgeores.2017.04.017. Publisher Copyright: © 2017.

Werner, C.L., Wegmüller, U., Strozzi, T., Wiesmann, A., 2000. Gamma sar and interferometric processing software. In: ERS-ENVISAT Symposium.

Wright, T.J., Parsons, B.E., Lu, Z., 2004. Toward mapping surface deformation in three dimensions using insar. Geophys. Res. Lett. 31. https://doi.org/10.1029/2003GL018827.

Wu, S., Zhang, B., Liang, H., Wang, C., Ding, X., Zhang, L., 2021. Detecting the deformation anomalies induced by underground construction using multiplatform mt-insar: a case study in to kwa wan station, Hong Kong. IEEE J. Sel. Top. Appl. Earth Obs. Remote Sens. 14, 9803–9814. https://doi.org/10.1109/JSTARS.2021.3113672.

Zhao, Q., Ma, G., Wang, Q., Yang, T., Liu, M., Gao, W., Falabella, F., Mastro, P., Pepe, A., 2019. Generation of long-term insar ground displacement time-series through a novel multi-sensor data merging technique: the case study of the Shanghai coastal area. ISPRS J. Photogramm. Remote Sens. 154, 10–27. https://doi.org/10.1016/j.isprsjprs.2019.05.005.